

ARTICLE OPEN

Topological superconducting phase in high- T_c superconductor MgB_2 with Dirac–nodal-line fermionsKyunghwan Jin¹, Huaqing Huang¹, Jia-Wei Mei^{1,2}, Zheng Liu³, Lih-King Lim³ and Feng Liu^{1,4}

Topological superconductors are an intriguing and elusive quantum phase, characterized by topologically protected gapless surface/edge states residing in a bulk superconducting gap, which hosts Majorana fermions. Unfortunately, all currently known topological superconductors have a very low transition temperature, limiting experimental measurements of Majorana fermions. Here we discover the existence of a topological Dirac–nodal-line state in a well-known conventional high-temperature superconductor, MgB_2 . First-principles calculations show that the Dirac–nodal-line structure exhibits a unique one-dimensional dispersive Dirac–nodal line, protected by both spatial-inversion and time-reversal symmetry, which connects the electron and hole Dirac states. Most importantly, we show that the topological superconducting phase can be realized with a conventional *s*-wave superconducting gap, evidenced by the topological edge mode of the MgB_2 thin films showing chiral edge states. Our discovery may enable the experimental measurement of Majorana fermions at high temperature.

npj Computational Materials (2019)5:57; <https://doi.org/10.1038/s41524-019-0191-2>

INTRODUCTION

Superconducting and topological states are among the most fascinating quantum phenomena in nature. The entanglement of these two states in a solid material into a topological superconducting state will give rise to even more exotic quantum phenomena, such as Majorana fermions. Recently, much effort has been devoted to searching for topological superconductors (TSCs). The first way to realize a TSC phase is by the proximity effect via formation of a heterojunction between a topological material and a superconductor (SC).^{1–3} Cooper pairs can tunnel into a topological surface state (TSS), forming a localized state that hosts Majorana bound states at magnetic vortices,^{1–3} or into a spin-polarized TSS, leading to half-integer quantized conductance.⁴ Second, TSCs can be made by realizing superconductivity in a topological material^{5–11} or conversely by identifying the topological phase in a superconductor.^{12–15} Broadly speaking, it is preferred to work with one single material, because interfacing two materials may suffer from the interface reaction and lattice mismatch between a SC and a topological material. Regardless of which approach to create a TSC, however, a common challenge is that all the known TSCs to date have a very low transition temperature. For example, up to now, a few superconducting/topological heterostructures are realized with low critical temperature (T_c) ~ 4 K.³ The superconducting transition temperature induced by doping and/or pressurizing a few topological insulators has a T_c in the range of 4–9 K,^{5–11} while the T_c for some materials where topological and superconducting phases coexist is <7 K.^{12–14} High-temperature two-dimensional (2D) SC FeSe on a SrTiO_3 substrate has recently been shown to also host a 2D topological insulating phase with hole doping, whereas its superconducting phases require electron doping.¹⁵

Here, we discover the existence of a topological phase in a conventional SC of MgB_2 with a T_c of ~ 40 K, the highest transition temperature known for a bulk BCS SC. Based on first-principles calculations, we demonstrate a topological Dirac nodal line (DNL)^{16–18} structure in MgB_2 , exhibiting a unique combination of topological and superconducting properties. The characteristic 1D-dispersive DNL is shown to be protected by both spatial-inversion and time-reversal symmetry, which connects the electron and hole Dirac states. A topological surface band of the (010) surface of MgB_2 shows a highly anisotropic band dispersion, crossing the Fermi level within the superconducting gap. The essential physics of the DNL structure in MgB_2 is further analyzed by effective tight-binding (TB) models, and the effects of superconducting transition on thin films are also studied. Most importantly, Majorana edge mode, having protected chiral bands crossing zero energy, can be realized.

RESULTS AND DISCUSSION

MgB_2 has the AlB_2 -type centrosymmetric crystal structure with the space group $P6/mmm$ (191). As shown in Fig. 1a, it is a layered structure with alternating close-packed trigonal layers of Mg, while B layers form a primitive honeycomb lattice like graphene. The optimized lattice constants are $a = 3.074$ Å and $c = 3.518$ Å, which agree well with the experimental^{19,20} and other theoretical results.^{21,22} The first Brillouin zone (BZ) of bulk MgB_2 and the projected surface BZ of the (010) plane are shown in Fig. 1b.

To reveal the electronic and topological properties of MgB_2 , its electronic band structure is calculated with or without spin–orbit coupling (SOC) (see Supplementary Information). Figure 1c, d shows the dominant bonding character of the B sheet and the bulk band structure of MgB_2 with SOC, respectively. The band

¹Department of Materials Science and Engineering, University of Utah, Salt Lake City, UT 84112, USA; ²Institute for Quantum Science and Engineering, and Department of Physics, Southern University of Science and Technology, 518055 Shenzhen, China; ³Institute for Advanced Study, Tsinghua University, 100084 Beijing, China and ⁴Collaborative Innovation Center of Quantum Matter, 100084 Beijing, China
Correspondence: Feng Liu (fliu@eng.utah.edu)

Received: 9 November 2018 Accepted: 26 March 2019

Published online: 03 May 2019

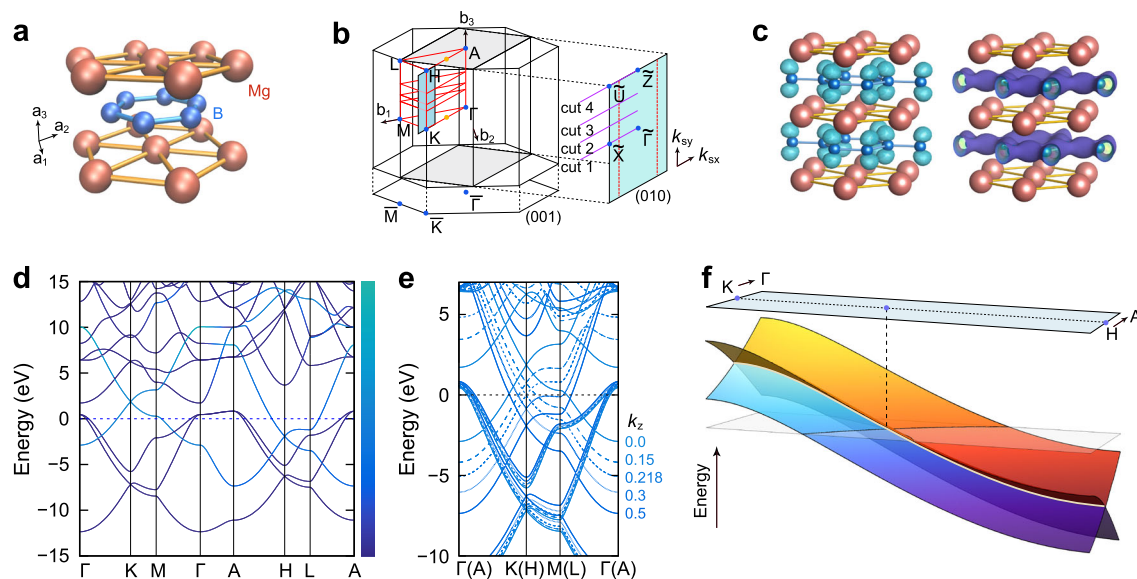


Fig. 1 Crystal and electronic structure of MgB_2 . **a** Crystal structure of MgB_2 with $P6/mmm$ symmetry. **b** Bulk BZ and the projected BZ of the (010) and (001) surface with purple lines indicating the locations of cuts 1–4 for surface states in Fig. 2a. **c** π ($B p_z$) and σ ($B s, p_{x,y}$) bonding character of boron sheet. **d** Band structure of MgB_2 with the coded bonding character. The color gradient from purple to blue represents a varying contribution from σ bonding to π bonding of boron sheet. **e** Band structure along high-symmetry points which are located in the same plane as varying the k_z value. **f** Dispersive Dirac nodal line structure along the K–H direction as indicated by a small cyan rectangle in **b**

structure exhibits linear dispersions at both K and H point. The resulting band structure can be easily understood in terms of the B sublattice. The bonding character of the bands in Fig. 1d is indicated by a color gradient. Dirac bands are derived from B p_z states (π -bonding) like the graphene Dirac state and other three bands below Dirac bands are from B $p_{x,y}$ states (σ -bonding).²¹ Mg s states are pushed up by the B p_z orbitals and donate fully their electrons to the B-derived conduction bands. All bands from B s and p orbitals are highly dispersive, the bands from σ -bonding are more localized in a 2D B sheet (no dispersion along the z direction), while the Dirac bands are quite isotropic with high dispersion along the z direction. Substantial k_z dispersion of the p_z bands produces a Fermi surface that is approximately mirror reflected with respect to a plane between the $k_z = 0$ [in units of $2\pi/c$] and $k_z = 0.5$ planes, with one pocket (electron-like) coming from the antibonding and the other (hole-like) from the bonding p_z band.

Remarkably, the Dirac bands are also dispersive along the K–H directions, so that we have a dispersive Dirac–nodal-line structure (Fig. 1e, f). Figure 1e shows the band structure along the high-symmetry points that are located in the same plane as k_z is varied. At $k_z = 0$, there is a hole-doped Dirac band with a Dirac-point energy of 1.87 eV, while at $k_z = 0.5$, there is an electron-doped Dirac band with a Dirac-point energy of -1.91 eV. As k_z increases, the hole-doped Dirac state changes to the electron-doped Dirac state continuously, and the critical point is located at $k_{zc} = 0.218$, where the carrier changes sign. Usually, SOC may open up gaps at the band crossing points; inversion and/or time-reversal symmetry is insufficient to protect the band crossings. But additional symmetry, like nonsymmorphic symmetry, can protect nodal points or lines. For MgB_2 , the Dirac nodal line is protected by crystal symmetry and SOC may introduce a small gap, leading to a topological insulating phase. However, the SOC strength of B is negligibly small ($\sim \mu\text{eV}$), even weaker than C and N. Consequently, the topological nodal line of MgB_2 survives by a combination of inversion, time-reversal, and crystal symmetries, along with a weak SOC of B. We note that MgB_2 also has a nodal chain structure²³ among the conduction or valence bands (see Supplementary Information), but these states are located far from the Fermi level.

We define two independent topological Z_2 indices denoted by ζ_1 and ζ_2 ,²⁴ one on a closed loop wrapping around the nodal line and the other on a cylinder enclosing the whole line, respectively (Fig. S2). The expression of ζ_1 is described by the Berry phase, $\phi = \oint_C d\vec{k} \cdot \vec{A}(\vec{k})$, as a line integral along a closed path

$$\zeta_1 = \frac{1}{\pi} \oint_C d\vec{k} \cdot \vec{A}(\vec{k}), \quad (1)$$

where $\vec{A}(\vec{k})$ is the Berry connection, $\vec{A}(\vec{k}) = i\langle n | \nabla | n \rangle$. The simplest Hamiltonian near the K(K') point for the Dirac nodal line of MgB_2 is

$$h(\vec{k}) = v_F(k_x\sigma_x + k_y\sigma_y) + a\cos(k_z)\sigma_0, \quad (2)$$

where σ_i are Pauli matrices. For any path in the (k_x, k_y) -plane that goes around the Dirac line, the index ζ_1 is 1, which means the Dirac lines are stable against perturbations. For the topological invariant of the Dirac nodal line, one can calculate the index ζ_2 using the flow of Wannier charge centers on a set of loops covering the enclosing manifold.^{25,26} For the DNL in MgB_2 , the index ζ_2 is 0. But the nodal lines cannot shrink to a point, instead, they appear in pairs and can only be annihilated in pairs.²⁷ Furthermore, the parities of energy states can be used to assign the Z_2 topological invariants in topological Dirac nodal line semimetals. We found that MgB_2 is characterized by weak Z_2 indices²⁸ (see Table S1).

To further reveal the topological nature of the Dirac–nodal-line–semimetal (DNLS) state in MgB_2 , we also calculate the surface states. The existence of TSSs and Fermi arcs is one of the most important signatures of DNLS. Figure 2 shows the calculated surface-state spectrum of Mg-terminated (010) MgB_2 surface using an iterative Green's function method. We calculated the band dispersions perpendicular to the $\vec{\Gamma} - \vec{Z}$ direction with four representative cuts at different k_{sy} values in the surface BZ, whose momentum locations are indicated in Fig. 1b. As the bulk BZ is projected onto the (010) surface BZ, one can expect that the nodal line is located at $k_{sx} = 2/3$ along the symmetry line between $\vec{\Gamma}(\vec{Z})$ and $\vec{X}(\vec{U})$. The TSSs of DNLS connect two gapless Dirac points, which are the surface projections of the nodal points in the nodal line (Fig. 2a). Interestingly, as k_{sy} values increase, the type of bulk Dirac band is changed from the hole-doped to electron-doped. Accordingly, the TSSs connecting two Dirac points are also

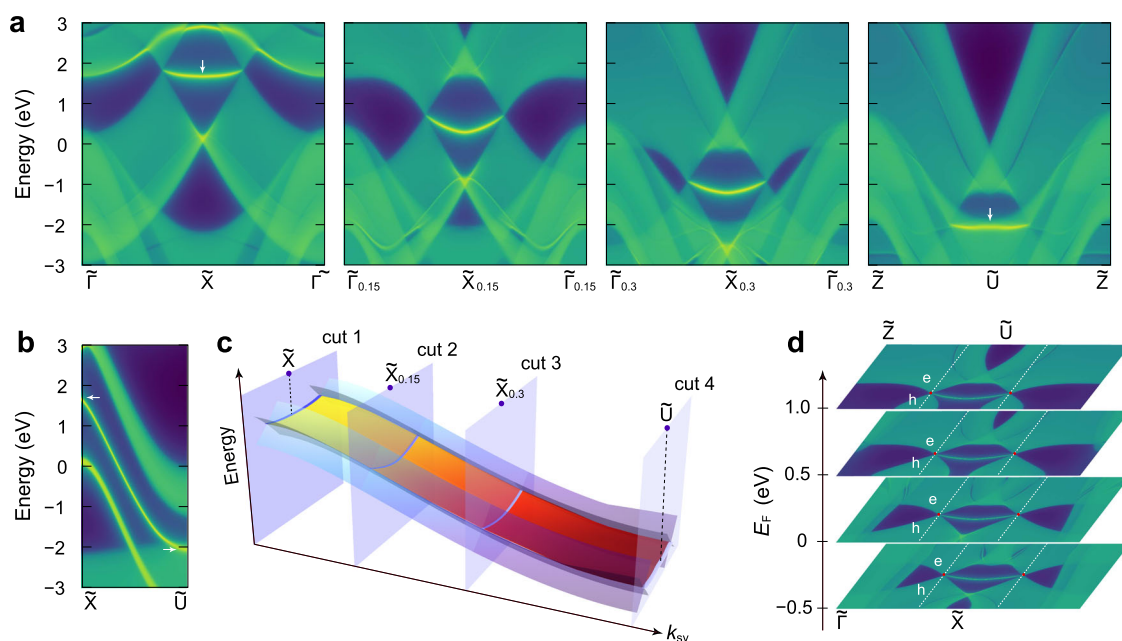


Fig. 2 Surface states of the MgB_2 (010) surface. **a** The projected density of state for Mg-terminated (010) surface along the cuts at $k_{sy} = 0, 0.15, 0.3$, and 0.5 in 2D surface BZ as indicated in Fig. 1b, respectively. **b** The surface states along the $\tilde{X} - \tilde{U}$ direction. **c** 3D schematic plot of the electronic surface band structure near two Dirac points. The gray planes indicate the momentum locations of cuts 1–4 in **a**. **d** Constant energy surface projection of bulk Dirac points

changed from hole to electron type. Moreover, these TSSs are quite anisotropic: the surface band dispersion is almost flat along the k_{sx} direction, but highly dispersive along the k_{sy} direction (Fig. 2a–c). The B-terminated surface states are shown in Fig. S3.

We now discuss the Fermi surface. The evolution of the Fermi surface is also obtained from the Green's function method for different values of Fermi energy (E_F) (Fig. 2d). The Fermi surface is composed of one Fermi arc, touching at two singularity points, where the surface projections of bulk Dirac points locate. The touching points which are indicated by red dots are also the jointed points between hole (h) and electron (e) pockets. As E_F increases, the touching point is shifted from $k_{sy} = 0.5$ [in units of $2\pi/c$] to $k_{sy} = 0$. Notably, we can observe the Fermi arc as long as E_F is between -1.91 eV and 1.87 eV. Such a large energy window for observing the Fermi arc is a unique and a useful feature of dispersive DNL in MgB_2 . Interestingly, beyond the electronic DNL state in MgB_2 , phononic Weyl nodal lines and their nontrivial phononic arc states were also predicted in MgB_2 .²⁹

The essential physics of the DNL structure in MgB_2 is further characterized by an effective TB model using B p_z orbital (see Supplementary Information), which gives a quite good description with density-functional theory (DFT) calculations (Fig. 3a). Given the DNL structure of MgB_2 , interesting features of quantum oscillation (the Shubnikov–de Hass or the de Haas–van Alphen effect) can be observed, to manifest the predicted nontrivial Berry phase.¹⁷ In graphene, such nonzero Berry phase has been confirmed.^{30,31} Similarly, the effective model of MgB_2 exhibits a pseudospin vortex texture arising from the band-degeneracy point (Fig. 3b). We note that the pseudospin is actually independent of k_z . One can clearly see the two inequivalent BZ corners (K and K') having different topologies and being characterized with opposite Berry phases. To measure the nontrivial Berry phase via Landau-fan-type analysis, the electron orbits should enclose the vortex points in a magnetic field. Figure 3c shows the calculated Fermi surface at different energy levels. For an undoped system, the electron and hole extremum orbits in a magnetic field along the z direction at E_F enclose the Γ point,

giving rise to a zero Berry phase. However, for a doped system, the Fermi surface topology changes for different doping levels. At $E_F = +1$ eV ($E_F = -1.2$ eV), the hole (electron) extremum orbit encloses the vortex point to enable a nonzero Berry phase (Fig. 3b, c). There are three different (energy) ranges of doping characterized with different Berry phases. If E_F locates at 0.29 eV $< E_F < 3.25$ eV (-3.48 eV $< E_F < -1.17$ eV), the hole (electron) extremum orbit encloses the vortex point for a nonzero Berry phase. For -1.17 eV $< E_F < 0.29$ eV, the electron (hole) extremum orbit excludes the vortex point having the zero Berry phase. Thus, to observe the nonzero Berry phase, electron or hole doping is needed. It is known that for MgB_2 , the Mg atoms can be substituted by Al to form $\text{Mg}_{1-x}\text{Al}_x\text{B}_2$, and B can be substituted by C to form $\text{Mg}(\text{B}_{1-y}\text{C}_y)_2$,^{32–34} to achieve electron doping. Using the rigid band and virtual crystal approximation, we have calculated the alloy band structures, which confirm an upward shifting of E_F due to electron doping (Fig. S4). The nontrivial Berry phase can be measured with a doping concentration of $x > 0.17$ or $y > 0.07$. Moreover, the biaxial compressive strain also induces electron doping in MgB_2 (Fig. S5).

On the one hand, our discovery of a topological state in MgB_2 might not appear surprising from the theoretical point of view, because of its similarity (the B hexagonal plane) to graphene/graphite. On the other hand, it is quite surprising from the experimental perspective, considering the fact that MgB_2 has been studied for over decades, but none of the experiments have detected any topological signature. This is because there are some fundamental differences between MgB_2 and graphene/graphite-based systems as we have revealed here. In particular, we show that in order to detect the topological signatures in MgB_2 , one has to do experiments differently from before, e.g., by measuring angle-resolved photoemission spectroscopy on the (001) instead of commonly used (111) surface and magnetoresistance in the doped sample instead of the intrinsic one. However, our most important discovery is possibly the topological superconducting state in MgB_2 as we discuss below.

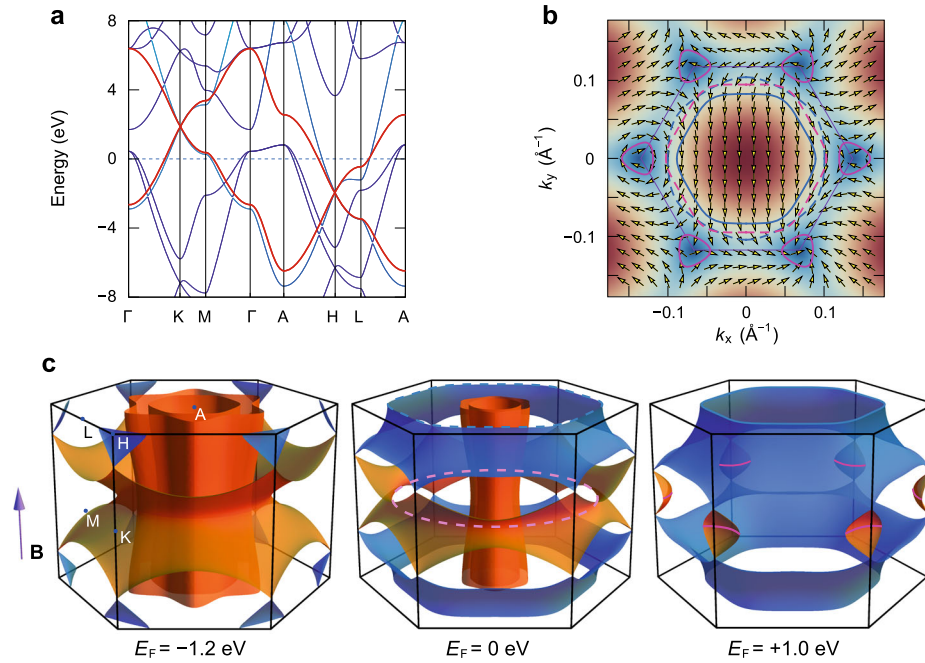


Fig. 3 Effective model of dispersive DNL of MgB_2 and Berry phase analysis. **a** The calculated band structure of an effective model (red lines) using B p_z orbitals with parameters $t = 1.50$ eV and $t_z = 0.954$ eV with DFT band structure. **b** The pseudospin texture with the corresponding valence energies. The arrows represent the pseudospin. The color gradient from red to blue represents energies of valence states. The blue and red dashed circles correspond to the electron and hole extremum orbits in a magnetic field (\mathbf{B}) along the z direction at $E_F = 0$ eV. The blue and red solid circle correspond to the electron and hole extremum orbits at $E_F = +1.0$ eV. **c** The Fermi surfaces for $E_F = -1.2$ eV, $E_F = 0$ eV, and $E_F = +1.0$ eV, respectively. The electron (hole) Fermi surfaces are indicated by blue (red) isosurfaces. The extremum orbits are indicated by a dashed line (solid line) for $E_F = 0$ eV ($E_F = +1.0$ eV)

We now consider the superconducting effect on DNLs. MgB_2 is a conventional BCS superconductor with two superconducting gaps, Δ_σ and Δ_π , which arise from the σ and π bands of the B electrons, respectively. The magnitude of the energy gap ranges from 1.5 to 3.5 meV for the π band and 5.5 to 8 meV for the σ band.^{35–41} The strong electron–phonon coupling is known in MgB_2 , as reflected by strong electron-pair formation of the σ -bonding states. Because the charge distribution of the σ -bonding states is not symmetrical with respect to the in-plane positions of boron atoms, the σ -bonding states couple very strongly to the in-plane vibration of boron atoms.³⁷ On the other hand, the π -bonding states, which are related with DNLs, form weaker pairs. However, this pairing is enhanced by the coupling to the σ -bonding states. Due to the coupling between π and σ states, π and σ gaps vanish at the same transition temperature $T_c \sim 39$ K, although their values are greatly different at low temperatures. Since the DNL in MgB_2 originates from the π band, we first consider the superconducting gap for the π band. But the promising TSC usually requires a spin-triplet (odd-parity) pairing state. For the bulk DNL with superconductivity, there is no spectral density in the s -wave superconducting gap (Fig. S6). In general, it is hard to realize the TSC phase using a bulk state.

To realize the TSC state, we now focused on the MgB_2 thin films. It was predicted that the MgB_2 thin films are mechanically stable and could be grown owing to the self-doping effect.⁴² Furthermore, few-monolayer MgB_2 has already been synthesized experimentally on some substrates.^{43–46} Figure 4 shows the band structure of MgB_2 (001) thin films. The dispersive DNL structure is projected onto a point and presented a formation of multiple Dirac states. These apparent Dirac states are also present in the surface bands for the two types of surface. The π states of the boron layer at the B-terminated (Mg-terminated) surface are indicated by red (blue) color. The Dirac state of the B-terminated surface shows hole type, while the Mg-terminated surface shows electron type. One can see that the Dirac state of the B-terminated

surface behaves independently. Moreover, the s -wave and multiple-gap superconductivity in MgB_2 thin films is retained up to a high critical temperature of 20–50 K.^{47,48} Taking advantage of these unique features of thin films, we can realize a 2D TSC state.

Conventional s -wave superconductivity has been utilized to generate TSCs via proximity to some materials.⁴⁹ The Dirac state in the boron layer of the B-terminated surface can be considered as the effective 2D hexagonal lattice model. To realize Majorana fermions with the s -wave superconducting gap, we consider a hexagonal lattice TSC based on a model of boron layer with Rashba SOC and exchange field. The corresponding TB Hamiltonian is given by

$$H = -t \sum_{\langle i,j \rangle a} c_{ia}^\dagger c_{ja} + i\lambda_R \sum_{\langle i,j \rangle a\beta} (\boldsymbol{\sigma}_{a\beta} \times \mathbf{d}_{ij})_z c_{ia}^\dagger c_{j\beta} + V_z \sum_{ia} c_{ia}^\dagger \sigma_z c_{ia} + \Delta_\pi \sum_i (c_{i1}^\dagger c_{i1}^\dagger + \text{H.c.}) - \mu \sum_{ia} c_{ia}^\dagger c_{ia}, \quad (3)$$

where c_{ia}^\dagger (c_{ia}) is the creation (annihilation) operator on site i with spin α , and $\boldsymbol{\sigma}$ are the Pauli matrices. The $\langle i, j \rangle$ represents the nearest-neighboring (NN) sites. The first term is the NN hopping term in the boron layer. The second term is the Rashba SOC arising from a perpendicular electric field to the B layer adjacent to a substrate, with λ_R and \mathbf{d}_{ij} representing the coupling strength and a unit vector from site j to site i , respectively. The V_z (Δ_π) in the third (fourth) term corresponds to the exchange field (superconducting gap of the π band). The μ in the last term is chemical potential. We can transform the Hamiltonian of Eq. (3) to the Bogoliubov–de Gennes (BdG) Hamiltonian H_{BdG} in the momentum space (see Supplementary Information).

If neglecting the Rashba and exchange field term, the system is topologically trivial with a s -wave superconducting gap, which is the same as the bulk DNL state. As expected, the superconducting gap mixes the Dirac states, resulting in the disappearance of gapless edge modes. When the Rashba and exchange field are turned on, spin-up and spin-down bands are split and mixed. The

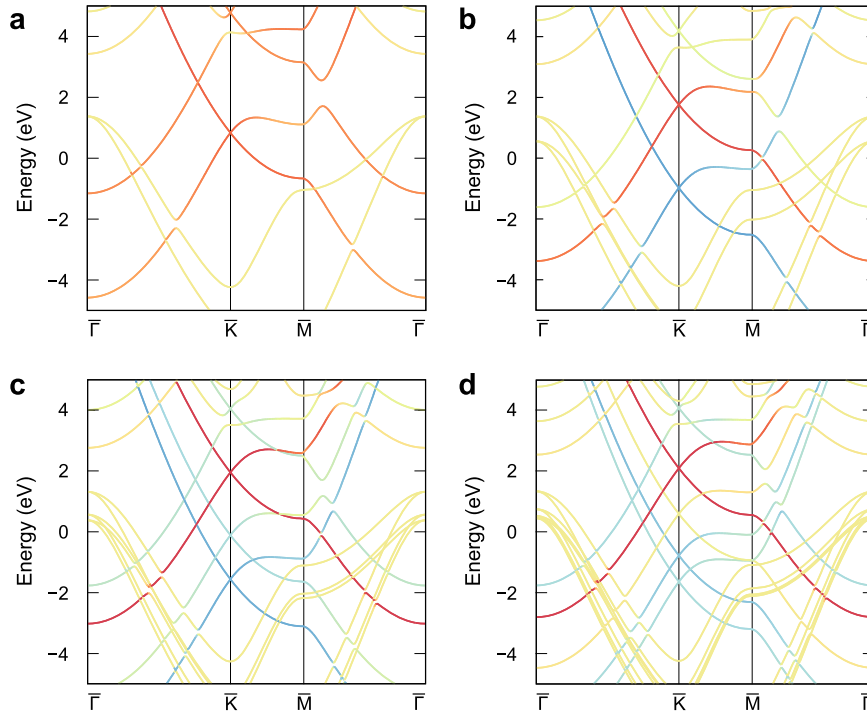


Fig. 4 Electronic structure of MgB₂ (001) thin films. **a–d** Calculated band structures of one, two, three, and four layers of MgB₂ (001) thin films, respectively. The red (blue) color represents the π state of the boron layer at the B-terminated (Mg-terminated) surface

2D BdG Hamiltonian with a broken time-reversal symmetry belongs to the topological class D,⁵⁰ which is characterized by an integer number. The Chern number C_1 can be calculated by⁵¹

$$C_1 = \frac{1}{2\pi} \int_{\text{BZ}} d^2\vec{k} f_{xy}(\vec{k}), \quad (4)$$

where $f_{xy}(\vec{k})$ is the Berry curvature

$$f_{xy}(\vec{k}) = i \sum_{m,n} (f_m - f_n) \frac{u_{m\vec{k}}^\dagger \partial_{k_x} H_{\text{BdG}} u_{n\vec{k}} - u_{n\vec{k}}^\dagger \partial_{k_y} H_{\text{BdG}} u_{m\vec{k}}}{(E_{m\vec{k}} - E_{n\vec{k}})^2}. \quad (5)$$

Here, $u_{m\vec{k}}(E_{m\vec{k}})$ is the m th eigenvector (eigenvalue) of H_{BdG} ; f_m is Fermi occupation factor. Interestingly, we found that the boron layer of MgB₂ thin film is topologically nontrivial in the case of $|V_z| \geq |\Delta_\pi|$ with the Chern number $C_1 = 4$. We note that this criterion does not depend on the value of the Rashba coupling. Figure 5a shows the calculated energy spectrum of BdG Hamiltonian near the crossing points with different V_z values. We have chosen the pairing Δ_π as 3 meV, similar to the experimental s -wave gap in MgB₂. For a pristine hexagonal boron layer, the Dirac bands appear at the \bar{K} and \bar{K}' points, respectively. If the exchange and Rashba SOC interactions are considered, the trivial s -wave superconducting gap near the Dirac point turns into a topological gap. As the magnetic exchange field V_z increases, the topological gap increases. Further, we study the topological phase diagram as shown in Fig. 5b. The bandgap (E_g) is calculated in the (k_x, k_y) -plane. The phase boundary between the normal SC and TSC is determined by the dashed curves, i.e., $V_z = \Delta_\pi$. To visualize the formation of TSSs within the superconducting gap, we calculated the Majorana edge states with a semiinfinite boron sheet. Figure 5c, d shows the energy spectra of the zigzag edge near the \bar{K} and \bar{K}' points. We found that there exist two zero-energy states in each valley with the same propagation direction ($v_F < 0$), which is in agreement with $C_1 = 4$. This indicates that these zero-energy states are topologically protected Majorana edge states. An armchair edge also exhibits four protected bands crossing zero energy (Fig. S8).

Finally, we address the experimental feasibility of the TSC from a quantum anomalous Hall (QAH) phase of graphene having a similar structural system with the boron layer. Graphene on the magnetic insulator, such as BiFeO₃,⁵² RbMnCl₃,⁵³ and Cr₂Ge₂Te₆,⁵⁴ can have an exchange field ($V_z \sim 70$ – 240 meV) and Rashba SOC ($\lambda_R \sim 1$ – 4 meV), realizing the QAH state. We suggest that MgB₂ thin films be epitaxially grown on these magnetic substrates, and the exchange field and Rashba SOC can be induced in the boron layer adjacent to the substrate. Since the MgB₂ thin films naturally have s -wave superconductivity, the MgB₂ thin films are expected to become TSC with the induced exchange field ($V_z \geq \Delta_\pi$) and Rashba SOC.

In summary, based on first-principles calculations and model analysis, an intriguing inversion and time-reversal symmetry-protected Dirac nodal line state is revealed in a high-temperature superconductor MgB₂. Our finding provokes an exciting opportunity to study a topological superconducting phase in an unprecedented high temperature and may offer a promising material platform to building novel quantum and spintronics devices. It will stimulate future studies of topological phases in a broader range of superconducting materials, such as a honeycomb lattice layered structure.

METHODS

We performed first-principles calculations within the framework of density-functional theory (DFT) using the Perdew–Burke–Ernzerhof-type generalized gradient approximation (GGA) for the exchange–correlation functional, as implemented in the Vienna ab initio simulation package.^{55,56} All the calculations are carried out using the kinetic energy cutoff of 500 eV on a $12 \times 12 \times 12$ Monkhorst–Pack k -point mesh. All structures are fully optimized until the residual forces are less than 0.01 eV/Å. The SOC is included in the self-consistent electronic structure calculation. We construct Wannier representations by projecting the Bloch states from the first-principles calculation of bulk materials onto Mg s and B s, p orbitals.⁵⁷ Based on Wannier representations, we further calculate the surface density of states and Fermi surface using the surface Green's function method for the (010) surface of a semiinfinite system.^{58,59}

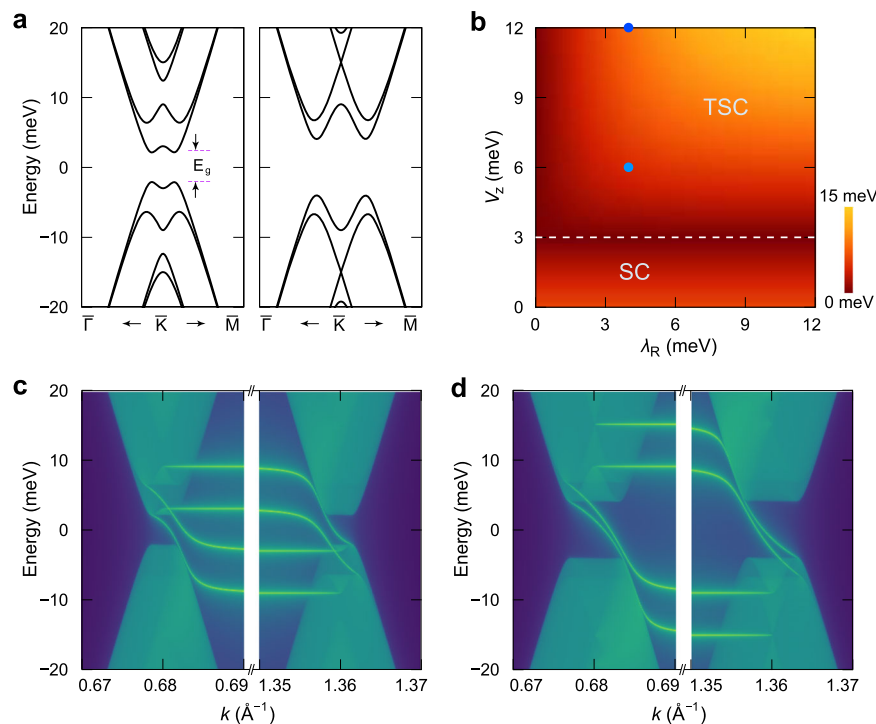


Fig. 5 The topological edge mode of the MgB_2 thin films. **a** The calculated band structure of the BdG Hamiltonian with parameters $t = 1.5$ eV, $\mu = 0$ eV, $\Delta_\pi = 3$ meV, $\lambda_R = 4$ meV, $V_z = 6$ meV (left), and $V_z = 12$ meV (right), respectively. **b** Topological phase diagram in the parameter space of λ_R and V_z . The color indicates the bandgap (E_g) in the (k_x, k_y) -plane at $k_z = 0.25$. The band structure parameters for **a** are marked by the dot. The dashed line is the boundary between normal SC and TSC. **c, d** The calculated edge spectra for the zigzag edge of the semiinfinite boron sheet with parameters in **a**, respectively

DATA AVAILABILITY

The data that support the findings of this study are available from the corresponding authors upon reasonable request.

ACKNOWLEDGEMENTS

We would like to thank Tomáš Ždušek, QuanSheng Wu, and Alexey A. Soluyanov for helpful discussions. K.-H.J., H.H., and F.L. acknowledge financial support from DOE-BES (No. DE-FG02-04ER46148). We also thank the Supercomputing Center at NERSC and CHPC at the University of Utah for providing the computing resources.

AUTHOR CONTRIBUTIONS

K.J. and F.L. designed the research. K.J. performed theoretical calculation, H.H., J.M., Z.L., and L.L. discussed the results, and K.J. and F.L. prepared the paper.

ADDITIONAL INFORMATION

Supplementary information accompanies the paper on the *npj Computational Materials* website (<https://doi.org/10.1038/s41524-019-0191-2>).

Competing interests: The authors declare that they have no competing interests.

Publisher's note: Springer Nature remains neutral with regard to jurisdictional claims in published maps and institutional affiliations.

REFERENCES

- Fu, L. & Kane, C. L. Superconducting proximity effect and Majorana fermions at the surface of a topological insulator. *Phys. Rev. Lett.* **100**, 096407 (2008).
- Akhmerov, A. R., Nilsson, J. & Beenakker, C. W. J. Electrically detected interferometry of Majorana fermions in a topological insulator. *Phys. Rev. Lett.* **102**, 216404 (2009).
- Wang, M.-X. et al. The coexistence of superconductivity and topological order in the Bi_2Se_3 thin films. *Science* **336**, 52–55 (2012).
- Stern, A. Non-Abelian states of matter. *Nature* **464**, 187–193 (2010).
- Hor, Y. S. et al. Superconductivity in $\text{Cu}_x\text{Bi}_2\text{Se}_3$ and its implications for pairing in the undoped topological insulator. *Phys. Rev. Lett.* **104**, 057001 (2010).
- Wray, L. A. et al. Observation of topological order in a superconducting doped topological insulator. *Nat. Phys.* **6**, 855 (2010).
- Sasaki, S. et al. Topological superconductivity in $\text{Cu}_x\text{Bi}_2\text{Se}_3$. *Phys. Rev. Lett.* **107**, 217001 (2011).
- Sato, T. et al. Fermiology of the strongly spin-orbit coupled superconductor $\text{Sn}_{1-x}\text{In}_x\text{Te}$: implications for topological superconductivity. *Phys. Rev. Lett.* **110**, 206804 (2013).
- Zhang, J. L. et al. Pressure-induced superconductivity in topological parent compound Bi_2Te_3 . *PNAS* **108**, 24–28 (2011).
- Kirshenbaum, K. et al. Pressure-induced unconventional superconducting phase in the topological insulator Bi_2Se_3 . *Phys. Rev. Lett.* **111**, 001 (2013).
- Zhao, L. et al. Emergent surface superconductivity in the topological insulator Sb_2Te_3 . *Nat. Commun.* **6**, 8279 (2015).
- Sakano, M. et al. Topologically protected surface states in a centrosymmetric superconductor $\beta\text{-PdBi}_2$. *Nat. Commun.* **6**, 8595 (2015).
- Guan, S.-Y. et al. Superconducting topological surface states in the non-centrosymmetric bulk superconductor PbTaSe_2 . *Sci. Adv.* **2**, e1600894 (2016).
- Lv, Y.-F. et al. Experimental signature of topological superconductivity and Majorana zero modes on $\beta\text{-PdBi}_2$ thin films. *Sci. Bull.* **62**, 852–856 (2017).
- Wang, Z. F. et al. Topological edge states in high-temperature superconductor $\text{FeSe}/\text{SrTiO}_3$ (001) film. *Nat. Mater.* **15**, 968–973 (2016).
- Burkov, A. A. & Hook, M. D., & Balents, L. Topological nodal semimetals. *Phys. Rev. B* **84**, 235126 (2011).
- Kim, Y., Wieder, B. J., Kane, C. L. & Rappe, A. M. Dirac line nodes in inversion-symmetric crystals. *Phys. Rev. Lett.* **115**, 806 (2015).
- Yu, R., Weng, H., Fang, Z., Dai, X. & Hu, X. Topological node-line semimetal and Dirac semimetal state in antiperovskite Cu_3PdN . *Phys. Rev. Lett.* **115**, 036807 (2015).
- Jones, M. E. & Marsh, R. E. The preparation and structure of magnesium boride, MgB_2 . *J. Am. Chem. Soc.* **76**, 1434–1436 (1954).
- Nagamatsu, J., Nakagawa, N., Muranaka, T., Zenitani, Y. & Akimitsu, J. Superconductivity at 39 K in magnesium diboride. *Nature* **410**, 63–64 (2001).
- Kortus, J., Mazin, I. I., Belashchenko, K., Antropov, V. P. & Boyer, L. L. Superconductivity of metallic boron in MgB_2 . *Phys. Rev. Lett.* **86**, 4656 (2001).

22. Liu, A. Y., Mazin, I. I. & Kortus, J. Beyond Eashberg superconductivity in MgB_2 : anharmonicity, two-phonon scattering, and multiple gaps. *Phys. Rev. Lett.* **87**, 087005 (2001).
23. Bzdušek, T. et al. Nodal-chain metals. *Nature* **538**, 75–78 (2016).
24. Fang, C., Weng, H., Dai, X. & Fang, Z. Topological nodal line semimetals. *Chin. Phys. B* **25**, 117106 (2016).
25. Bzdušek, T. & Sigrist, M. Robust doubly crged nodal lines and nodal surfaces in centrosymmetric systems. *Phys. Rev. B* **96**, 155105 (2017).
26. Fang, C., Chen, Y., Kee, H.-Y. & Fu, L. Topological nodal line semimetals with and without spin-orbital coupling. *Phys. Rev. B* **92**, 081201 (2015).
27. Hyart, T., Ojajarvi, R. & Heikkilä, T. T. Two topologically distinct dirac-line semi-metal phases and topological phase transitions in rhombohedrally stacked honeycomb lattices. *J. Low. Temp. Phys.* **191**, 35–48 (2018).
28. Fu, L. & Kane, C. L. Topological insulators with inversion symmetry. *Phys. Rev. B* **76**, 045302 (2007).
29. Xie, Q. et al. Phononic weyl nodal straight lines in high-temperature superconductor MgB_2 . *arXiv:1801.04048* (2018).
30. Novoselov, K. S. et al. Two-dimensional gas of massless Dirac fermions in graphene. *Nature* **438**, 197–200 (2005).
31. Zhang, Y., Tan, Y.-W., Stormer, H. L. & Kim, P. Experimental observation of the quantum Hall effect and Berry's phase in graphene. *Nature* **438**, 201–204 (2005).
32. de la Peña, O., Aguayo, A. & de Coss, R. Effects of Al doping on the structural and electronic properties of $\text{Mg}_{1-x}\text{Al}_x\text{B}_2$. *Phys. Rev.* **66**, 012511 (2002).
33. Wilke, R. H. T. et al. Systematic effects of carbon doping on the superconducting properties of $\text{Mg}(\text{B}_{1-x}\text{C}_x)_2$. *Phys. Rev. Lett.* **92**, 217003 (2004).
34. Kortus, J., Dolgov, O. V., Kremer, R. K. & Golubov, A. A. Band filling and interband scattering effects in MgB_2 : carbon versus aluminum doping. *Phys. Rev. Lett.* **94**, 027002 (2005).
35. Szabó, P. et al. Evidence for two superconducting energy gaps in MgB_2 by point-contact spectroscopy. *Phys. Rev. Lett.* **87**, 137005 (2001).
36. Giubileo, F. et al. Two-gap state density in MgB_2 : a true bulk property or a proximity effect? *Phys. Rev. Lett.* **87**, 177008 (2001).
37. Choi, H. J., Roundy, D., Sun, H., Cohen, M. L. & Louie, S. G. The origin of the anomalous superconducting properties of MgB_2 . *Nature* **418**, 758–760 (2002).
38. Eskildsen, M. R. et al. Vortex imaging in the π band of magnesium diboride. *Phys. Rev. Lett.* **89**, 187003 (2002).
39. Souma, S. et al. The origin of multiple superconducting gaps in MgB_2 . *Nature* **423**, 65–67 (2003).
40. Xi, X. X. Two-band superconductor magnesium diboride. *Rep. Prog. Phys.* **71**, 116501 (2008).
41. Iavarone, M. et al. Two-band superconductivity in MgB_2 . *Phys. Rev. Lett.* **89**, 187002 (2002).
42. Tang, H. & Ismail-Beigi, S. Self-doping in boron sheets from first principles: a route to structural design of metal boride nanostructures. *Phys. Rev. B* **80**, 134113 (2009).
43. Cepek, C. et al. Epitaxial growth of MgB_2 (0001) thin films on magnesium single-crystals. *Appl. Phys. Lett.* **85**, 976 (2004).
44. Petaccia, L. et al. Characterization of high-quality MgB_2 (0001) epitaxial films on $\text{Mg}(0001)$. *New J. Phys.* **8**, 12 (2006).
45. Bekaert, J. et al. Free surfaces recast superconductivity in few-monolayer MgB_2 : combined first-principles and ARPES demonstratn. *Sci. Rep.* **7**, 14458 (2017).
46. Cheng, S.-H. et al. Fabrication and characterization of superconducting MgB_2 thin film on graphene. *AIP Adv.* **8**, 075015 (2018).
47. Morshedloo, T., Roknabadi, M. R. & Behdani, M. First-principles study of the superconductivity in MgB_2 bulk and in its bilayer thin film based on electron-phonon coupling. *Phys. C* **509**, 1–4 (2015).
48. Bekaert, J., Aperis, A., Partoens, B., Oppeneer, P. M. & Milošević, M. V. Evolution of multigap superconductivity in the atomically thin limit: Strain-enhanced three-gap superconductivity in monolayer MgB_2 . *Phys. Rev. B* **96**, 094510 (2017).
49. Lutchyn, R. M., Sau, J. D. & Das Sarma, S. Majorana fermions and a topological phase transition in semiconductor-superconductor heterostructures. *Phys. Rev. Lett.* **105**, 077001 (2010).
50. Schnyder, A. P., Ryu, S., Furusaki, A. & Ludwig, A. W. W. Classification of topological insulators and superconductors in three spatial dimensions. *Phys. Rev. B* **78**, 195125 (2008).
51. Ghosh, P., Sau, J. D., Tewari, S. & Das Sarma, S. Non-Abelian topological order in noncentrosymmetric superconductors with broken time-reversal symmetry. *Phys. Rev. B* **82**, 184525 (2010).
52. Qiao, Z. et al. Quantum anomalous Hall effect in graphene proximity coupled to an antiferromagnetic insulator. *Phys. Rev. Lett.* **112**, 116404 (2014).
53. Zhang, J., Zhao, B., Yao, Y. & Yang, Z. Quantum anomalous Hall effect in graphene-based heterostructure. *Sci. Rep.* **5**, 10629 (2015).
54. Zhang, J., Zhao, B., Yao, Y. & Yang, Z. Robust quantum anomalous Hall effect in graphene-based van der Waals heterostructures. *Phys. Rev. B* **92**, 165418 (2015).
55. Kresse, G. & Furthmüller, J. Efficient iterative schemes for *ab initio* total-energy calculations using a plane-wave basis set. *Phys. Rev. B* **54**, 11169 (1996).
56. Perdew, J. P., Burke, K. & Ernzerhof, M. Generalized gradient approximation made simple. *Phys. Rev. Lett.* **77**, 3865 (1996).
57. Mostofi, A. A. et al. wannier90: A tool for obtaining maximally-localised Wannier functions. *Comput. Phys. Commun.* **178**, 685 (2008).
58. Sancho, M. P. L., Sancho, J. M. L. & Rubio, J. Quick iterative scheme for the calculation of transfer matrices: application to Mo (100). *J. Phys. F* **14**, 1205 (1984).
59. Wu, Q., Zhang, S., Song, H.-F., Troyer, M. & Soluyanov, A. A. WannierTools: an open-source software package for novel topological materials. *Comput. Phys. Commun.* **224**, 405 (2018).



Open Access This article is licensed under a Creative Commons Attribution 4.0 International License, which permits use, sharing, adaptation, distribution and reproduction in any medium or format, as long as you give appropriate credit to the original author(s) and the source, provide a link to the Creative Commons license, and indicate if changes were made. The images or other third party material in this article are included in the article's Creative Commons license, unless indicated otherwise in a credit line to the material. If material is not included in the article's Creative Commons license and your intended use is not permitted by statutory regulation or exceeds the permitted use, you will need to obtain permission directly from the copyright holder. To view a copy of this license, visit <http://creativecommons.org/licenses/by/4.0/>.

© The Author(s) 2019